EUROFUSION WPCD-PR(16) 15919

A Stegmeir et al.

Advances in the flux-coordinate independent approach

Preprint of Paper to be submitted for publication in
Computer Physics Communications

This work has been carried out within the framework of the EUROfusion Consortium and has received funding from the Euratom research and training programme 2014-2018 under grant agreement No 633053. The views and opinions expressed herein do not necessarily reflect those of the European Commission.

Advances in the flux-coordinate independent approach

Andreas Stegmeir[a], Omar Maj[a], David Coster[a], Karl Lackner[a], Markus Held[b], Matthias Wiesenberger[b]

[a]*Max-Planck-Institut für Plasmaphysik, D-85748 Garching, Germany*
[b]*Institute for Ion Physics and Applied Physics, University of Innsbruck, Technikerstrasse 25, A-6020 Innsbruck, Austria*

Abstract

The flux-coordinate independent approach (FCI) offers a promising solution to deal with a separatrix and X-point(s) in diverted tokamaks. Whereas the discretisation of perpendicular operators (with respect to magnetic field) is straight forward, the major complexity lies in the discretisation of parallel operators, for which field line tracing and interpolation is employed. A discrete version for the parallel diffusion operator was proposed in [1], which maintains the self-adjointness property on the discrete level and exhibits only very low numerical perpendicular diffusion/pollution. However, in situations where the field line map is strongly distorted this scheme revealed its limits. Moreover, the appearance of small scale corrugations deteriorated the convergence order with respect to spatial resolution [2]. In this paper we present an extension to the scheme where the parallel gradient is reformulated via a combination of integration and interpolation. It is shown that the resultant scheme finally combines many good numerical properties, i.e. it is self-adjoint on the discrete level, it has very low numerical perpendicular diffusion, it can cope with strongly distorted maps and exhibits optimal convergence. Another subtle issue in the FCI approach is the treatment of boundary conditions, especially where magnetic field lines intersect with material plates. We present a solution based on ghost points, whose value can be set in a flexible way according to Taylor expansion around the boundary.

Keywords: Flux-coordinate independent approach, field line map, support operator method

1. Introduction

The geometry of diverted magnetic fusion devices poses a challenge to the numerical treatment of the plasma edge and scrape-off layer (SOL). Dynamics in tokamaks is usually strongly anisotropic leading to structures which are strongly elongated along magnetic field lines ($k_\parallel \ll k_\perp$). This flute mode character is usually exploited computationally in numerical codes via employing field-aligned coordinate systems [3] and sparsifying the computational grid along the resulting parallel coordinate. However, field/flux-aligned coordinates become singular on the separatrix/X-point(s) and therefore codes based on these coordinates cannot span a simulation domain across the separatrix. The flux-coordinate independent approach (FCI) [4, 5, 6, 1] offers a solution to this dilemma: The simulation domain is spanned with a cylindrical grid, which is well defined everywhere in the region of interest, and the discretisation of perpendicular operators turns out to be straight forward. For the discretisation of parallel operators a field line map is used: Parallel operators are discretised via a finite difference along magnetic field lines, for which field line tracing towards neighbouring poloidal planes is performed and required values on the field line are obtained by interpolation. Finally, the flute mode character can be exploited computationally by sparsifying the grid along the toroidal direction. The FCI approach allows a high flexibility in geometry and is used in few codes, like FENICIA [5], GRILLIX [1], FELTOR [2], BOUT++ [7]. It has been successfully applied to hyperbolic and parabolic problems.

The main complexity of the approach lies in the discretisation of parallel operators, and a major critical issue is numerical perpendicular diffusion/pollution caused by the interpolation which couples distinct magnetic field lines. The highly anisotropic dynamics, e.g. the ratio of parallel to perpendicular heat conductivity may reach levels of $\chi_\parallel/\chi_\perp \sim 10^{10}$, implies that even a small directional error of discrete parallel operators may overwhelm the real slow perpendicular dynamics. Following the method of support operators [8, 9] numerical schemes for the parallel diffusion operator were derived in [1, 10], which conserve the self-adjointness property on the discrete level and exhibit a highly reduced level of numerical diffusion as compared to a naive discretisation. Two types of schemes, one based on interpolation and another one based on integration were derived. However, it turned out that the schemes which are based on interpolation exhibit erroneous corrugations, especially in situations where the field line map is strongly distorted, i.e. at low toroidal resolutions and in presence of strong magnetic shear. Moreover, a deteriorated convergence behaviour was recently found from numerical tests in complicated geometries with $\nabla \cdot \mathbf{b} \neq 0$ [2], with $\mathbf{b}$ the magnetic field unit vector. In this paper we present an extension to these schemes, where the underlying parallel gradient is reformulated via a combination of interpolation and integration. We show that the resultant scheme combines many good numerical properties: It is self adjoint the discrete level, it has very low numerical perpendicular diffusion/pollution, it can cope even with strongly distorted field line maps and it exhibits the expected second order convergence with respect to toroidal resolution. Moreover, it is also

Email address: Andreas.Stegmeir@ipp.mpg.de (Andreas Stegmeir)

very practical as it does not require substantial additional effort in implementation and it does not increase the computational cost.

Furthermore, we discuss the treatment of boundaries within the FCI approach. Especially at the intersection of magnetic field lines with material surfaces (limiter, divertor) subtle numerical problems may arise, as e.g. also information from outside the boundary is required for interpolation and the distances from grid points to the boundary may vary strongly. We present in this paper a solution which is based on ghost points, whose values are set according to a Taylor expansion along magnetic field lines around the boundary. This offers a simple and flexible way to deal with different kinds of boundary conditions.

All developed methods were implemented in the code GRILLIX, with which the presented numerical tests were carried out.

2. Parallel operators within FCI approach

A general introduction into the FCI approach, which is reviewed here only shortly, can be found e.g. in [4, 5, 6, 1] and we focus on the discretisation of parallel operators. We consider in the following an axisymmetric tokamak configuration which is spanned by a cylindrical grid (R_i, Z_j, φ_k), which is Cartesian with grid spacing h within poloidal planes k. Based on the assumption of a strong toroidal field ($B_{tor} \gg B_{pol}$) perpendicular operators can be approximated with a stencil which remains within these Cartesian poloidal planes, and their discretisation is straight forward as e.g. standard finite difference methods could be used. In order to exploit the flute mode character ($k_\parallel \ll k_\perp$) the resolution in the toroidal direction is sparsified and a field line following discretisation for parallel operators is used. For each grid point (R_i, Z_j) a field line tracing towards the neighbouring poloidal planes $k \pm 1$ is performed yielding its map points $(R^\pm_{i,j}, Z^\pm_{i,j})$ and the corresponding arc lengths along the field line $\Delta s^\pm_{i,j}$. Due to axisymmetry this information is independent on the toroidal grid index k.

2.1. Parallel gradient

A finite difference along magnetic field lines can be used to obtain a discrete version for the parallel gradient. The value for some quantity u at the map points, i.e $u^\pm_{i,j,k} := u(R^\pm_{i,j}, Z^\pm_{i,j}, k \pm 1)$, are computed thereby via interpolation as the map points do not in general coincide with grid points. The forward/backward finite difference $\mathbf{Q}^\pm$ of the parallel gradient follows as [1] (see fig. 1):

$$(\mathbf{Q}^\pm u)_{i,j,k} := \pm \frac{u^\pm_{i,j,k} - u_{i,j,k}}{\Delta s^\pm_{i,j}}. \tag{1}$$

For evaluation of the parallel gradient at the grid point itself (R_i, Z_j, φ_k) a linear interpolation of the forward/backward expression along magnetic field lines is proposed:

$$(\mathbf{Q}u)_{i,j,k} := \frac{(\mathbf{Q}^+u)_{i,j,k}\,\Delta s^-_{i,j} + (\mathbf{Q}^-u)_{i,j,k}\,\Delta s^+_{i,j}}{\Delta s^+_{i,j} + \Delta s^-_{i,j}} \tag{2}$$

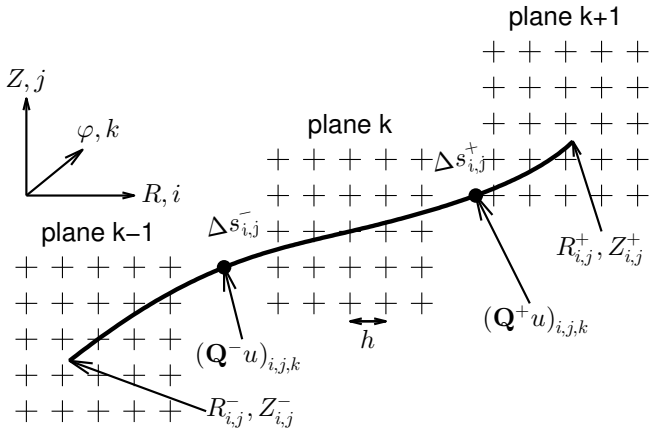

Figure 1: Scheme for computation of parallel gradient based on interpolation within FCI approach.

The interpolation couples distinct field lines, which causes numerical perpendicular diffusion/pollution, which can be controlled by the order of interpolation. A higher order interpolation exhibits less numerical perpendicular diffusion but has a larger stencil and might be more prone to oscillations (Runge's phenomenon).

Especially around the X-point and at low toroidal resolutions the field line map can be strongly distorted, i.e. field lines of two neighbouring grid points spread apart such that the distance between neighbouring map points is large ($> h$). A sketch of this situation (reduced to two dimensions) is shown in fig. 2a. In reality any parallel dynamics would spread information across many grid points in between neighbouring map points in a smooth way. However, the discrete parallel gradient according to definition (1) only connects the considered grid point to those points which are actually involved in the interpolation. It was shown in [1] that this may cause erroneous corrugations if adjacent map points are far apart. Two remedies to this were also suggested in [1]: The first one is simply to require enough toroidal resolution to bring the map distortion below a quantifiable threshold and the second one is to change the parallel gradient to account for the map distortion via using the integral formulation of the parallel gradient, i.e.:

$$\nabla_\parallel u = \lim_{V\to 0} \frac{1}{BV} \int_{\partial V} u\mathbf{B} \cdot d\mathbf{S}, \tag{3}$$

On the discrete level we use toroidally limited flux boxes as illustrated in fig. 2b, where the only contribution to the surface integral stems from the toroidal ends of the flux box volume.

$$(\mathbf{Q}^\pm u)_{i,j,k} := \pm \frac{1}{(\mathcal{V}B)^\pm_{i,j}} \left[\int_{A^\pm_{i,j}} uB_{tor} dA - \int_{A^0_{i,j}} uB_{tor} dA \right], \tag{4}$$

where $A^0_{i,j}$ is the base square of lateral length h around grid point i, j and $A^\pm_{i,j}$ its mapped area. The prefactor can be obtained with high accuracy from the field line tracing procedure

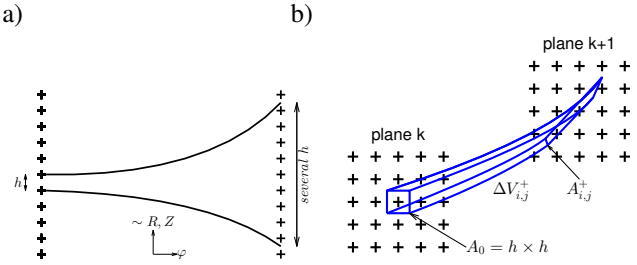

Figure 2: a) Sketch for map distortion (illustration reduced to two dimensions). b) Scheme for computation of parallel gradient based on integration. Finite flux box volume is plotted in blue

utilizing conservation of toroidal magnetic flux:

$$(\mathcal{V}B)^{\pm}_{i,j} = h^2 B_{tor}(R_i, Z_j) \int_0^{\pm\Delta\varphi} \frac{B(\gamma(\varphi))}{B_{tor}(\gamma(\varphi))} R d\varphi = h^2 B_{tor}(R_i, Z_j) \Delta s^{\pm}_{i,j}, \tag{5}$$

where $\gamma(\varphi)$ is the curve traced along magnetic field line with $\gamma(0) = \left(R_i, Z_j\right)$.

It was proposed in [1] to express the surface integrals on the discrete level via computing overlaps of the mapped quad with the base squares, and it was shown that problems caused by map distortion can be resolved by this in principle. However, since with this approach the representation of quantities in the perpendicular direction is of low order – quantities are assumed to be piecewise constant within base squares $[R_i - \frac{h}{2}, R_i + \frac{h}{2}] \times [Z_j - \frac{h}{2}, Z_j + \frac{h}{2}]$ – the numerical diffusion/pollution is high in comparison to a high order interpolation method. Moreover, the computation of the surface overlaps is cumbersome and for strongly distorted maps the overlap of not only quads but general polygons might have to be considered.

For a new improved scheme we propose to combine interpolation and integration. We split the two integrals of eq. (4) into $2^X \times 2^X$, $X \in \mathbb{N}_0$ subcells, and express them on the discrete level as (see fig. 3):

$$\int_{A^0_{i,j}} u B_{tor} dA = \frac{h^2}{2^X 2^X} \sum_{s,t=1}^{2^X} u(R_{ij_s}, Z_{ij_t}, \varphi_k) B_{tor}(R_{ij_s}, Z_{ij_t}) \tag{6}$$

$$\int_{A^{\pm}_{i,j}} u B_{tor} dA = \frac{h^2}{2^X 2^X} \sum_{s,t=1}^{2^X} u(R^{\pm}_{ij_s}, Z^{\pm}_{ij_t}, \varphi_{k\pm1}) B_{tor}(R_{ij_s}, Z_{ij_t}), \tag{7}$$

where

$$R_{ij_s} := R_i - \frac{h}{2} + \frac{h}{2^X}\left(s - \frac{1}{2}\right), \quad Z_{ij_t} := Z_j - \frac{h}{2} + \frac{h}{2^X}\left(t - \frac{1}{2}\right) \tag{8}$$

and $R^{\pm}_{ij_s}, Z^{\pm}_{ij_t}$ the corresponding map points. Again conservation of magnetic flux has been utilized to express the toroidal magnetic flux in the mapped area via the toroidal magnetic flux in the base area. The values $u(R_{ij_s}, Z_{ij_t}, \varphi_k)$ and $u(R^{\pm}_{ij_s}, Z^{\pm}_{ij_t}, \varphi_{k\pm1})$ are obtained via interpolation.

We make a few comments to the new scheme. If we consider the case $X = 0$, i.e. no splitting into subcells, the new scheme

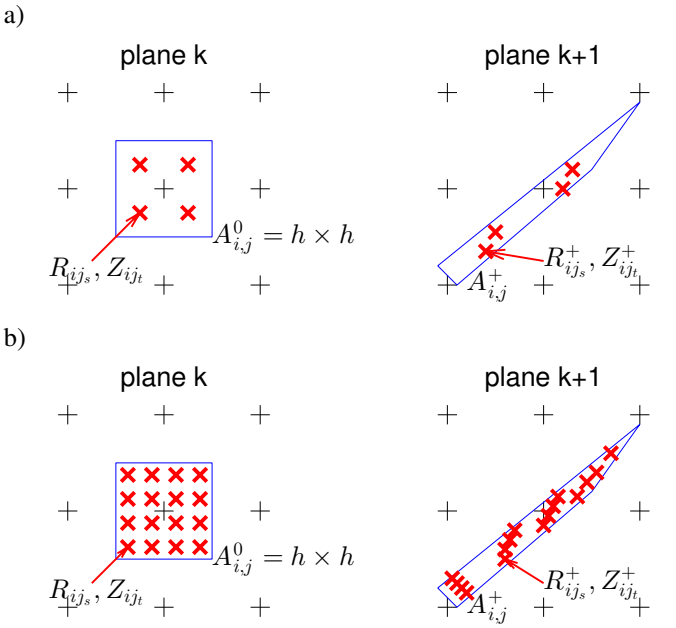

Figure 3: Sketch of integration-interpolation scheme for a) $X = 1$, i.e. splitting into four subcells, and b) $X = 2$, i.e. splitting into 16 subcells.

is identical to the pure interpolation scheme given in eq. (1). If the parameter X is increased the mapped area is traced out more precisely and stronger map distortions can be resolved. Provided that a field line tracing routine and an interpolation routine are already available, only very little additional effort in implementation is required as compared to the pure interpolation scheme. The computational effort for establishing the parallel gradients is of order $O\left(2^{2X}\right)$ as compared to the pure interpolation scheme. However, the discrete parallel gradients $\mathbf{Q}^{\pm}$ usually have to be established only once at the beginning of a simulation and remain then fixed in time. Concerning computational performance the critical part is finally the often repeated application of parallel operators. As the size of the final stencil is very similar to the pure interpolation scheme and not strongly dependent on X there is no significant increase in computational cost.

2.2. *Parallel diffusion*

We consider the parallel diffusion operator:

$$\mathcal{D}_{\parallel} u := \nabla \cdot \left[\mathbf{b} \nabla_{\parallel} u\right], \tag{9}$$

with $\mathbf{b}$ the unit vector of the magnetic field. Two different discrete versions for the parallel diffusion operator were suggested in [1, 10] which are reviewed here shortly.

For the first (naive) discretisation we rewrite $\mathcal{D}_{\parallel} u = \nabla^2_{\parallel} u + (\nabla \cdot \mathbf{b}) \nabla_{\parallel} u$ and apply a further finite difference on the discrete parallel gradient to obtain:

$$\left(\mathbf{D}^N u\right)_{i,j,k} := \frac{(\mathbf{Q}^+ u)_{i,j,k} - (\mathbf{Q}^- u)_{i,j,k}}{(\Delta s^+_{i,j} + \Delta s^-_{i,j})/2} + (\nabla \cdot \mathbf{b})_{i,j} (\mathbf{Q} u)_{i,j,k} \tag{10}$$

Note that in contrast to [1, 10] the scheme is extended by the second term, whereby $(\nabla \cdot \mathbf{b})_{i,j}$ can be computed directly from a given equilibrium.

The second scheme in [1, 10] followed the method of support operators [8, 9]. For simplicity we consider only real valued scalar fields which vanish at the boundary. Then the integral equality that we want to conserve on the discrete level is:

$$\int_V u\mathcal{D}_\parallel v dV = -\int_V \nabla_\parallel u \nabla_\parallel v dV, \tag{11}$$

which implies $\nabla \cdot [\mathbf{b}\circ] = -\nabla_\parallel^\dagger$ and $\mathcal{D}_\parallel = \mathcal{D}_\parallel^\dagger$. On the left hand side of eq. (11) is an integration over scalars and on the right hand side over fluxes, which are identified on the discrete level with distinct spaces. SG is the space of discrete scalar fields, which are collocated on the basic cylindrical grid (R_i, Z_j, φ_k), and $FG^\pm$ are the spaces of discrete fluxes which are collocated half way along magnetic field lines between neighbouring poloidal planes, i.e. on a staggered grid in the parallel sense (see fig. 1). Due to the '±' choice of the parallel gradient we have also two distinct spaces for the discrete fluxes. We define inner products in these discrete spaces:

$$\langle u, v\rangle_{SG} := \sum_\lambda u_\lambda v_\lambda \Delta V_\lambda, \quad \langle q^\pm, p^\pm\rangle_{FG^\pm} := \sum_\mu q^\pm_\mu p^\pm_\mu \Delta\mathcal{V}^\pm_\mu, \tag{12}$$

where Greek indices denote summation over all grid points. ΔV_λ and $\Delta\mathcal{V}^\pm_\mu$ are flux box volumes corresponding to the toroidal intervals $\left[\varphi_k - \frac{\Delta\varphi}{2}, \varphi_k + \frac{\Delta\varphi}{2}\right]$ respectively $[\varphi_k, \varphi_k \pm \Delta\varphi]$. The mapping of the discrete operators between these spaces is:

$$\mathbf{D}_\parallel : SG \to SG, \quad \mathbf{Q}^\pm : SG \to FG^\pm, \quad \tilde{\mathbf{Q}}^\pm : FG^\pm \to SG, \tag{13}$$

where $\mathbf{D}_\parallel$ is the discrete analogue of the parallel diffusion operator and $\tilde{\mathbf{Q}}^\pm$ the discrete analogue of the parallel divergence $\nabla \cdot [\mathbf{b}\circ]$, which we mention here for completeness although it is not needed explicitly in the following.

The discrete version for the parallel diffusion operator is derived from the discrete parallel gradient and by the requirement that the integral equality (11) holds on the discrete level:

$$\mathbf{D}^{supp}_{\parallel\lambda\sigma} = -\frac{1}{2}\left[\sum_\mu \mathbf{Q}^+_{\mu\lambda}\mathbf{Q}^+_{\mu\sigma}\frac{\Delta\mathcal{V}^+_\mu}{\Delta V_\lambda} + \sum_\mu \mathbf{Q}^-_{\mu\lambda}\mathbf{Q}^-_{\mu\sigma}\frac{\Delta\mathcal{V}^-_\mu}{\Delta V_\lambda}\right]. \tag{14}$$

The first '+' term alone is already a consistent version in itself as well as the second '−' term. However, to obtain a scheme which is independent of this arbitrary choice and therefore symmetric with respect to φ the average of both schemes is taken.

3. Numerical tests

For the following tests and examples a 3rd order bipolynomial interpolation was used to obtain values at points which do not coincide with grid points (e.g. map points). Therefore, 4×4 grid points centered around the considered point are used to obtain the interpolating polynomial. The following numerical schemes were investigated:

- **D-3**: Naive scheme for the parallel diffusion operator according to eq. (10). The discrete parallel gradient is thereby computed by pure interpolation ($X = 0$ or eq. (1)).
- **S-3X**X: Support scheme according to eq. (14) and parallel gradient according to eqs. (4), with terms therein given by eqs. (5) to (7). The parameter X, which controls the splitting into subcells is denoted by the number X.

We note that we found the naive method with the parallel gradient computed via interpolation-integration technique with $X > 0$ to be numerically unstable in some cases so we do not consider it here any further. This is another advantage of the support scheme as it guarantees a strict decrease of the L_2 norm and ensures therefore numerical stability [1].

3.1. Consistency

We investigate the convergence behaviour of the new schemes with a test case which was proposed in [2]. The magnetic field is axisymmetric:

$$\mathbf{B} = I_0\nabla\varphi + \nabla\psi\times\nabla\varphi, \tag{15}$$

with the poloidal magnetic field given in terms of the flux function.

$$\psi(R,Z) = \cos\left(\frac{R_0\pi}{2}(R-1)\right)\cos\left(\frac{R_0\pi}{2}Z\right), \tag{16}$$

which has $\nabla\cdot\mathbf{b} \neq 0$. We use as parameters $R_0 = 10$ and $I_0 = 20$, limit the simulation domain to $R \in [0.9, 1.1]$, $Z \in [-0.1, 0.1]$ and measure the numerical error of the discrete parallel diffusion operator in the L_2 and L_∞ norm:

$$\epsilon_n = \frac{\left|\mathbf{D}_\parallel\mathbf{u} - (\mathcal{D}_\parallel u)_h\right|_n}{\left|(\mathcal{D}_\parallel u)_h\right|_n}, \qquad n = 2, \infty, \tag{17}$$

where $(\mathcal{D}_\parallel u)_h$ is the analytic result collocated to grid points. The L_2 norm on the discrete level is induced by the discrete scalar product from eq. (12) (SG). We consider two test functions

$$u_1 = -\psi(R,Z)\cos\varphi = -\cos(5\pi(R-1))\cos(5\pi Z)\cos\varphi, \tag{18}$$

$$u_2 = -\cos(10\pi(R-1))\cos(10\pi Z)\cos\varphi, \tag{19}$$

In contrast to u_1, which has also been considered in [2], u_2 is more general as it is not aligned to flux surfaces within poloidal planes. For a convergence test we adapt the resolution in all three dimensions according to $\Delta\varphi = 2\pi\cdot 2^{-i}$, $h = \min\left\{10^{-2}, h_0\left(\frac{\Delta\varphi}{2\pi}\right)^{2/3}\right\}$, with $h_0 = 0.05$. This resolution sequence, i.e. a slightly slower grid refinement in the perpendicular direction than in the toroidal direction, was also employed in [2].

The numerical error for the test with function u_1 is shown in fig. 4 and the difference between the numeric and analytic result at resolution $\Delta\varphi = 2\pi/64$ in fig. 5. As already shown in [2] the naive scheme **D-3** converges with second order with respect to toroidal resolution, whereas the support scheme which is purely based on interpolation, i.e. **S-3X0**, exhibits an irregular and deteriorated convergence behaviour. As can be seen from fig. 5 this is due to few strong corrugations which appear

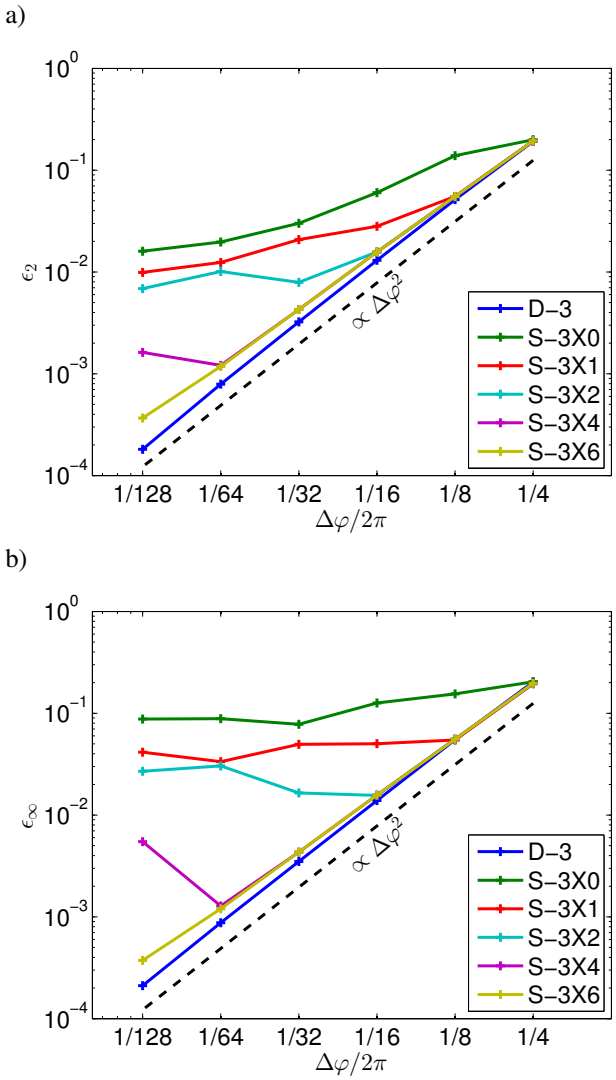

Figure 4: Numerical error in a) L_2 and b) L_∞ norm for test function u_1. Corresponding perpendicular resolution was $h = \min\left\{10^{-2}, h_0\left(\frac{\Delta\varphi}{2\pi}\right)^{2/3}\right\}$, with $h_0 = 0.05$.

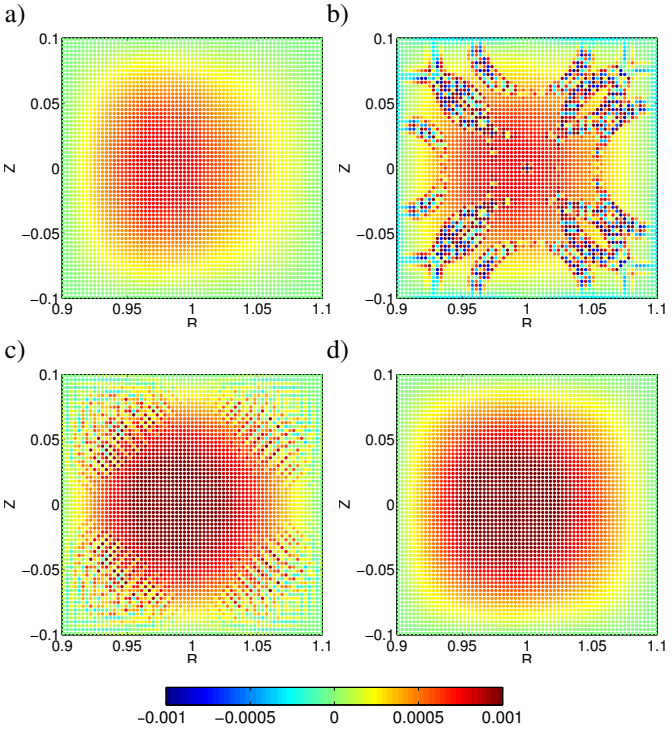

Figure 5: Difference between analytic and numeric parallel diffusion operator after action on u_1 at plane $\varphi = 0$ for resolution of $\Delta\varphi/2\pi = 1/64$, $h = 3 \cdot 10^{-3}$. a) **D-3**, b) **S-3X0** c) **S-3X2** and d) **S-3X6**.

if map points of two neighbouring grid points land in the same cell respectively jump across a grid cell (see appendix in [1] for a detailed example in a simplified setup). As the parameter X is increased these corrugations gradually vanish and a convergence order which is close to second order with respect to toroidal resolution is obtained. The same behaviour is also obtained for the more general function u_2 (see fig. 6). However, a strict second order convergence even with the **S-3X6** scheme is not obtained at the highest resolutions. This could possibly be resolved by taking into account the subcell structure also at the computation of the prefactors $(\mathcal{V}B)^{\pm}_{i,j}$ (see eq. (5)).

3.2. *Flute modes*

The tests from the previous section constitute unusual and extreme cases to the aligned schemes **D-3** and **S-3X**, since their true strength, especially of the support schemes, is finally

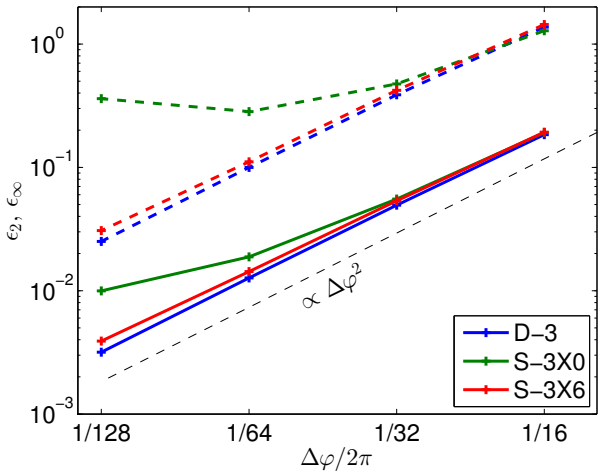

Figure 6: Numerical error in L_2 norm (solid) and L_∞ norm (dashed) for test function u_2.

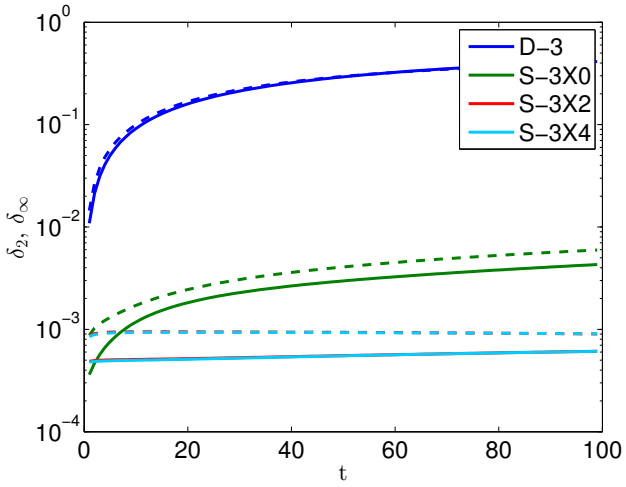

Figure 7: Temporal evolution of numerical error. A parallel diffusion equation was evolved in time with zonal mode $u(t = 0) = \sin\left(\frac{3}{2}\pi\psi\right)$ as initial state. The numerical errors δ_2 (solid) and δ_∞ (dashed) are here defined as $\delta_{2,\infty} = |\mathbf{u}(t) - \mathbf{u}(t = 0)|_{2,\infty} \,/\, |\mathbf{u}(t = 0)|_{2,\infty}$. The curves for the **S-3X2** (red) and **S-3X4** (cyan) practically overlap.

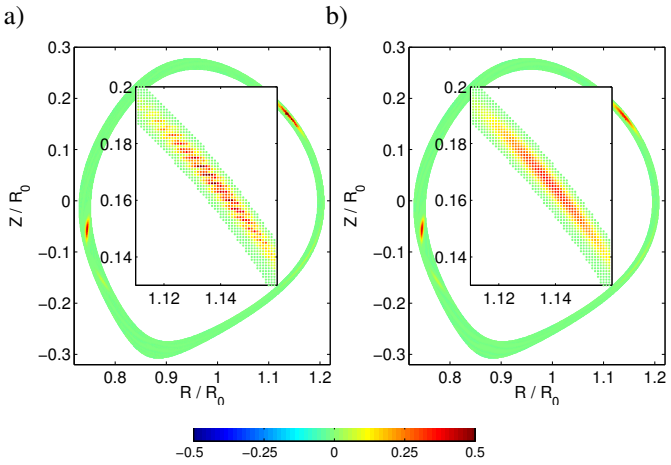

Figure 8: Example for distortion of map at low toroidal resolution $\Delta\varphi = 2\pi/2$. Perpendicular resolution was $h = 1 \cdot 10^{-3}$. Initial state was $u(R_i, Z_j, \varphi_k, t = 0) = \exp\left(-\frac{(R_i-0.88)^2+(Z_j+0.29)^2}{0.008^2}\right)\left(\frac{2\pi}{\Delta\varphi}\delta_{k0}\right)$. Result on plane $\varphi = \pi$ and time $t = 10$ for a) **S-3X0** and b) **S-3X2** scheme. Insets show top right region enlarged.

deployed for flute modes, i.e. structures which are strongly elongated along magnetic field lines ($k_\parallel \ll k_\perp$). The aligned schemes allow an accurate treatment of flute modes already at very low toroidal resolutions, whereas with non-aligned schemes a dense resolution in all three spatial dimensions is required [2].

The simplest example of a flute mode is a zonal structure, i.e. $u = u(\psi)$ for which $k_\parallel = 0$. We consider in the following the time dependent parallel diffusion equation:

$$\frac{\partial}{\partial t} u = \mathcal{D}_\parallel u, \tag{20}$$

and initialize the simulation as $u(t = 0) = \sin\left(\frac{3}{2}\pi\psi\right)$, which is a steady state. Therefore, any temporal evolution is due to numerical error, i.e. numerical perpendicular diffusion/pollution. In fig. 7 an example for the temporal evolution is shown. It is evident that the numerical diffusion/pollution is orders of magnitude lower for the support schemes than for the naive scheme. Whereas this has already been shown in [1, 10] it also holds true for the new scheme based on integration-interpolation. Moreover, we observe even less numerical diffusion than with the pure interpolation scheme.

At low toroidal resolution and strong magnetic shear the map might become strongly distorted (see again section 2.1 and fig. 2). It was shown in [1] that this was causing corrugations for the support scheme based on pure interpolation (**S-3X0**). As the new scheme based firstly on integration maps areas, problems arising from map distortion are easily resolved by increasing the parameter X. Fig. 8 illustrates an example for this, where an equilibrium from [11] was employed representing ASDEX Upgrade. The parallel diffusion equation (20) was evolved in time with a blob, i.e a Gaussian on a single poloidal plane, as initial state. A very low toroidal resolution of only two poloidal planes was used and a region of strong magnetic shear close to the separatrix was considered. The blob extends along magnetic field lines yielding a flute mode. With the **S-3X0** scheme erroneous corrugations arise, whereas the solution obtained with the **S-3X2** scheme is obviously smooth. We note that a non-aligned scheme would probably fail at such low toroidal resolutions (see also [2]), since the magnetic geometry sampled by the resolutions would not be resolved well. In contrast the aligned schemes (**D-3**, **S-3X**) resolve the geometry accurately due to tracing field lines.

3.3. Role of perpendicular resolution

The perpendicular resolution h determines the accuracy of the interpolation. During diffusion of a structure along magnetic field lines, magnetic shear gradually deforms its poloidal cross section, i.e. stretching it into one direction and compressing it into the other. In fig. 9 the poloidal cross section of a Gaussian blob after parallel diffusion to time $t = 5$ is shown, where the result of the 32 employed poloidal planes is superimposed. The blob was initialized on the outboard midplane and the deformation of its cross section towards the inside of the torus is clearly visible. Eventually the width of the structure goes below the perpendicular resolution h, where the interpolation becomes inaccurate. At this point either the perpendicular resolution has to be increased or some perpendicular dynamics, e.g. perpendicular dissipation, takes over.

In fig. 10 a view of the structure and its parallel derivative along the field line passing through the center of the blob is shown. At low perpendicular resolution ($h = 5 \cdot 10^{-4}$) corrugations are visible especially after passing a region of strong shear in the vicinity of the X-point ($x_\parallel/R_0 \lesssim -3$). The corrugations decrease as the perpendicular resolution is increased. Alternatively a perpendicular hyper-diffusion, e.g. of the type $\nu\nabla_\perp^6 u$ also reduces corrugations without affecting the global result significantly.

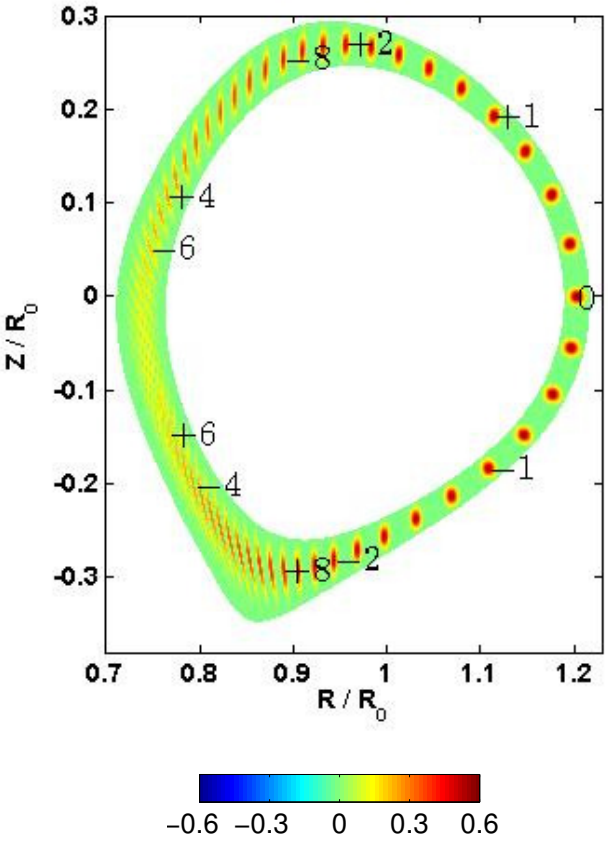

Figure 9: Result of diffusion of Gaussian blob $\left(u(R_i, Z_j, \varphi_k, t=0) = \exp\left(-\frac{(R_i-1.203)^2+Z_j^2}{0.007^2}\right)\left(\frac{2\pi}{\Delta\varphi}\delta_{k0}\right)\right)$ computed with **S-3X2** scheme. Superposition of 32 poloidal planes at $t = 5$ is shown. Numbers refer to length measured along field line starting from outboard midplane (As reference for fig. 10). Perpendicular resolution was $h = 5 \cdot 10^{-5}$.

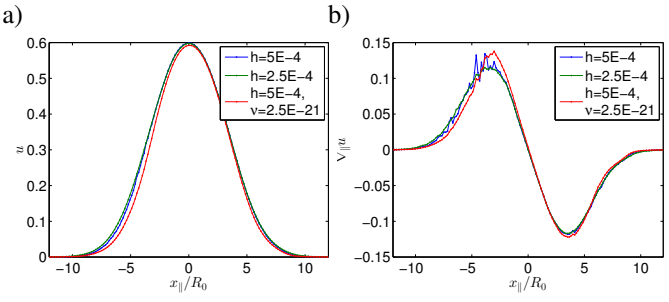

Figure 10: a) Quantity u and b) corresponding parallel gradient $\nabla_\parallel u$ illustrated along field line passing through center of blob from simulation of fig. 9 at $t = 5$. Simulations with low (blue), high (green) perpendicular resolution and a simulation with additionally hyperdiffusion of $\nu\nabla_\perp^6 u$ (red) were performed.

X	creation time [s]	evaluation time [s]	fill density of $\mathbf{Q}^\pm$ [%]
0	13.03	4.71	$5.97 \cdot 10^{-3}$
1	27.24	5.71	$8.23 \cdot 10^{-3}$
2	80.17	5.91	$8.85 \cdot 10^{-3}$
4	1156.14	6.01	$9.35 \cdot 10^{-3}$

Table 1: Time required for creation and evaluation of parallel operators in dependence on parameter X. Also the average fill density of the matrices $\mathbf{Q}^\pm$ is given.

3.4. Computational costs

The simulation from the previous section 3.3 $\left(h = 5 \cdot 10^{-4}\right)$ serve as test case to compare the computational cost of the new scheme in dependence on the parameter X. We profiled separately the creation of the parallel operators, i.e. the matrices $\mathbf{Q}^\pm$ which remained fixed in time, and the evaluation of $\mathbf{D}_\parallel^{supp}$ averaged over ≈ 400 applications. GRILLIX is MPI parallelized over the toroidal direction and OpenMp parallelized within poloidal planes, and the results were obtained on a parallel computing cluster with 32 MPI processes and one OpenMp thread per process (poloidal plane). The results are summarized in table 1. Whereas the time required for the creation increases strongly with the parameter X (towards $O\left(2^{2X}\right)$), the time for the evaluation does not increase substantially as also the size of the stencil which is represented by the fill density of the matrices $\mathbf{Q}^\pm$. The creation is usually done only once at the beginning of a simulation and the critical part concerning the performance is the evaluation, which is executed subsequently very often. Therefore, the overall computational cost does not increase significantly with X.

4. Boundaries within FCI

A subtle issue within the FCI approach is the treatment of boundaries, especially where magnetic field lines intersect with material plates, since these may have an immediate effect on the whole simulation domain. In general the intersection of field lines with boundaries can be identified during the field line tracing procedure.

An obvious problem arises if a map point is close to the boundary such that the standard interpolation stamp, (e.g. 4×4 centered around the map point for third order bipolynomial interpolation), extends across the boundary. Adapting the interpolation technique for such special cases can be cumbersome and the quality of interpolation might degrade. A simple and flexible approach consists of extending the domain by ghost points. Assuming that some reasonable extension for the magnetic field exists outside the domain, which is usually the case in practice, also an extension of parallel operators to ghost points is possible and fits very well into the established framework. Finally, just suitable values have to be assigned to ghost points. We discuss in the following only ghost points that are actually relevant for the parallel boundary conditions at the intersection of magnetic field lines with material surfaces, i.e. limiter or divertor plates. For other ghost points near the limiting flux surfaces where magnetic field lines are tangential to the boundary, we

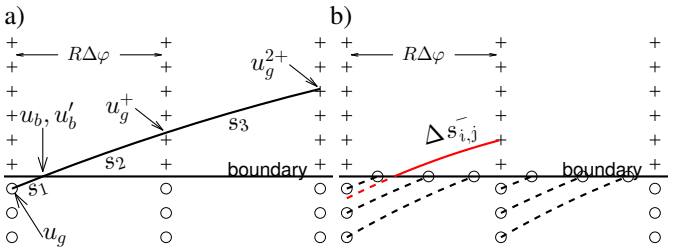

Figure 11: Scheme for treatment of boundary conditions. Crosses are grid points and open circles ghost points. a) For the case of Neumann boundary conditions a Taylor expansion along magnetic field lines around the intersection point is performed. b) For Dirichlet boundary conditions one may consider ghost points to be actually located on the boundary projected (black dashed) along magnetic field lines. Finite distances and volumes are adapted close to boundary (red).

assume that some suitable perpendicular boundary condition is available. In the following values on those ghost points are set to zero.

4.1. Neumann and Robin boundary conditions

A sketch for the treatment of Neumann boundary conditions is illustrated in fig. 11a. The computational grid is extended by ghost points located within poloidal planes. No adaption is required for the extension of discrete parallel operators to ghost points: The standard interpolation-integration procedure according to eqs. (6) and (7) is used, and the finite distances $\left(\Delta s_{i,j}^{\pm}\right)$ and volumes $\left(\Delta V_{i,j}, \Delta \mathcal{V}_{i,j}^{\pm}\right)$ are computed without respecting the boundary. Neumann boundary conditions at the intersection of the magnetic field line with the boundary are enforced by assigning values to the ghost points according to a second order Taylor expansion along magnetic field lines around the intersection point:

$$u_g = \frac{s_1^2 - s_3^2}{s_2^2 - s_3^2} u_g^+ + \frac{s_2^2 - s_1^2}{s_2^2 - s_3^2} u_g^{2+} - \frac{(s_1 + s_2)(s_1 + s_3)}{s_2 + s_3} u_b', \quad (21)$$

where u_g^+ is the value of the quantity at the mapped position from the considered ghost point at the next plane and u_g^{2+} the value at the next but one poloidal plane. Here s_1, s_2 and s_3 are the distances from these points to the boundary and u_b' is the prescribed parallel gradient at the intersection of the magnetic field line with the boundary. The expression for the $'-'$ direction follows analogously. The expansion up to second order takes into account a variation in the distance to the boundary, which may range from approximately $s_1 \approx 0$ to $s_1 \approx R\Delta\varphi$. We want to note that Neumann boundary conditions are usually treated by imposing the prescribed flux directly to the discrete flux at the boundary (see section 4.3, first item, for such an approach with its deficiencies). However, by assigning values to ghost points according to eq. (21) the discrete fluxes at the boundary do not necessarily coincide exactly with the prescribed flux, but only converge to it with increasing resolution.

As an example we consider the parallel diffusion equation with a Robin-like boundary condition:

$$\nabla_\parallel u\Big|_b = \mp\alpha u|_b \quad (22)$$

at the divertor plates, with α a positive constant and the negative/positive sign corresponds to field lines directed towards/away from the divertor plates. Considering the boundary condition (22) was motivated from sheath boundary conditions [12]. Required values at the intersection with the divertor plates $u|_b$ are computed via linear extrapolation from the interior domain, such that:

$$u_b' = \mp\alpha \frac{s_3 u_g^+ - s_2 u_g^{2+}}{s_3 - s_2}. \quad (23)$$

As initial state we consider again a blob located at the outboard midplane in the scrape-off layer, where a horizontal divertor at $Z = -0.42$ is present. Fig. 12 shows a snapshot on the 32 employed poloidal planes superimposed for the case $\alpha = 1$. The setting of the ghost points according to eq. (21) results in a structure which is obviously smooth across the boundary, and in order to show that the desired boundary condition is actually fulfilled we show in fig. 13 the representation of the structure along the field line passing through the center of the blob. The curves for the quantity and its parallel derivative intersect at the outer divertor, and therefore fulfill the desired boundary condition ($\nabla_\parallel u\big|_b = u|_b$ at the outer divertor for the case $\alpha = 1$).

In fig. 14a the result at $t = 2$ for different values of α is illustrated. The general trend that with decreasing α the parallel gradient at the outer divertor decreases fulfills the expectations. However, especially for the case $\alpha = 0$ the value for the parallel gradient is overestimated as the values on ghost points drop spuriously. This behaviour appears to be due to an insufficient perpendicular resolution. As can be seen from the snapshot (fig. 12) the structure becomes strongly distorted due to magnetic shear caused in the vicinity of the X-point [13] and its width becomes very small towards the outer divertor. The values u_g^+ and u_g^{2+}, which determine the value at the ghost points, are obtained from interpolation which becomes inaccurate. Fig. 14b compares the result for the case $\alpha = 0$ simulated with high and low perpendicular resolution. At higher perpendicular resolution the result converges towards the prescribed boundary condition.

4.2. Dirichlet boundary conditions

It is advantageous to treat Dirichlet boundary conditions slightly differently from Neumann or Robin boundary conditions. Discrete parallel operators are adapted near the boundary, i.e. the interpolation-integration procedure is still carried out according to eqs. (6) and (7), but the boundary is now respected at the computation of finite distances and volumes, i.e. there is no contributions from behind the boundary to $\Delta s_{i,j}^{\pm}$, $\Delta V_{i,j}$ and $\Delta \mathcal{V}_{i,j}^{\pm}$. One may thus consider ghost points to be, projected along magnetic field lines, located directly on the boundary as illustrated in fig. 11b. In this way the integration-interpolation procedure has not to be adapted and the desired value on the boundary can be set explicitly without need for extrapolation, which might cause numerical instabilities (see section 4.3).

As an example we initialize a simulation with $u = 0$ in the

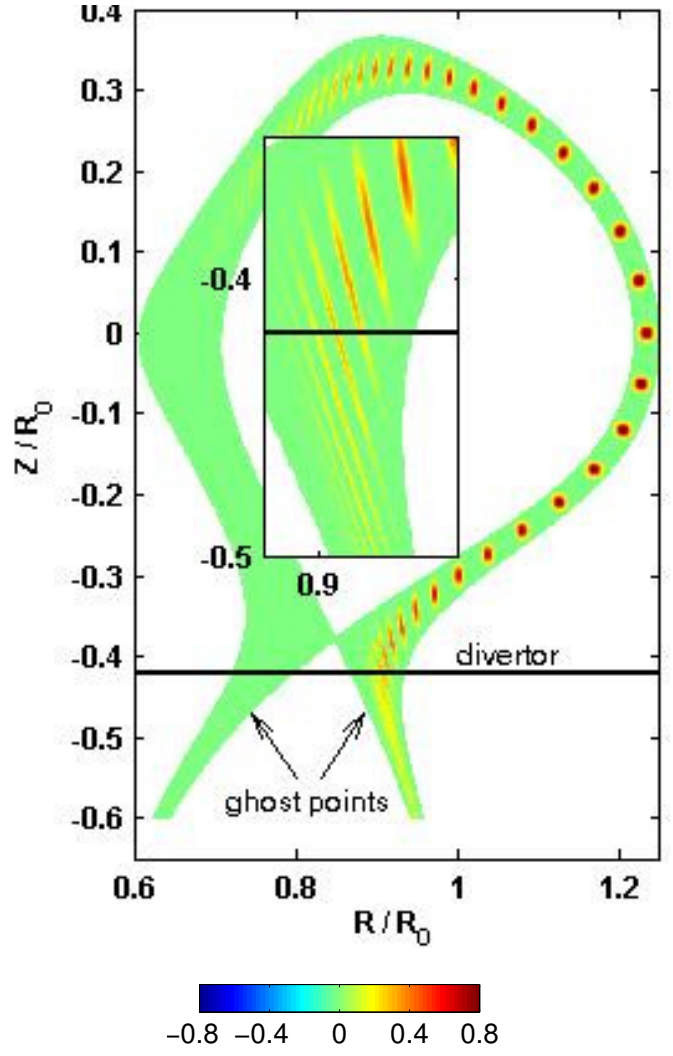

Figure 12: Snapshot of diffusion of Gaussian blob $\left(u(R_i, Z_j, \varphi_k, t=0) = \exp\left(-\frac{(R_i-1.233)^2+Z_j^2}{0.007^2}\right)\left(\frac{2\pi}{\Delta\varphi}\delta_{k0}\right)\right)$ at $t = 2$ for the case $\alpha = 1$. Result of $N_{pol} = 32$ poloidal planes is shown superimposed with inset showing the region around the boundary enlarged. Points below divertor, located horizontally at $Z = -0.42$ and indicated with thick black line, are ghost points, whose values are determined according to eq. (21). Perpendicular resolution was $h = 5 \cdot 10^{-4}$.

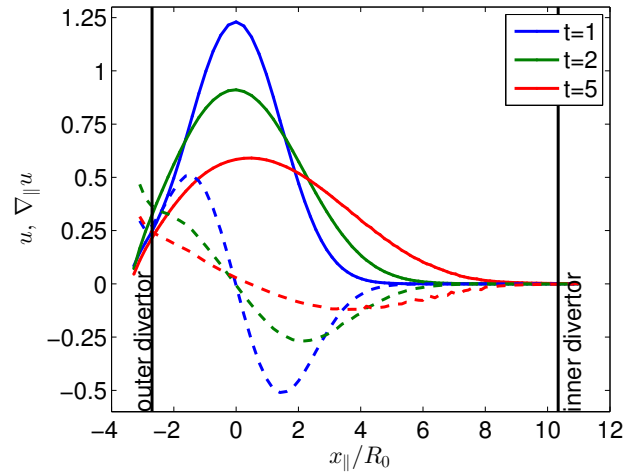

Figure 13: Representation of structure along magnetic field line passing through center of blob for the case $\alpha = 1$ at various times t. The quantity (solid) and its parallel derivative (dashed) are shown. At the inner divertor the quantity and its derivative intersect fulfilling the requested boundary condition $\nabla_\parallel u\big|_b = u|_b$.

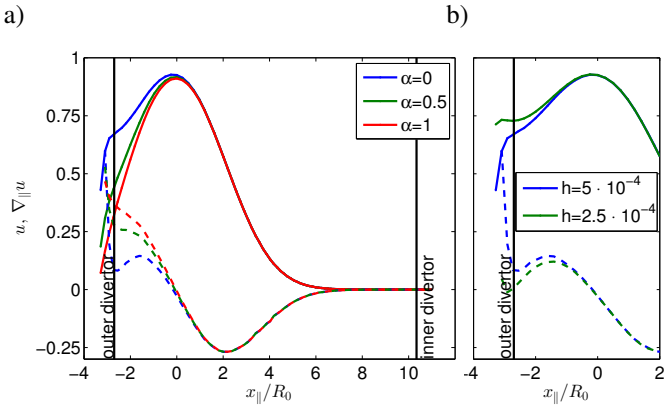

Figure 14: a) Quantity (solid) and its parallel derivative (dashed) along magnetic field line passing through center of blob at time $t = 2$ for different values of α. Especially for the case $\alpha = 0$ a spurious drop in the ghost point region of the outer divertor is obvious which leads to an overestimation of the parallel gradient. b) Comparison of simulation performed with low ($h = 5 \cdot 10^{-4}$) perpendicular resolution and high ($h = 2.5 \cdot 10^{-4}$) perpendicular resolution for the case $\alpha = 0$.

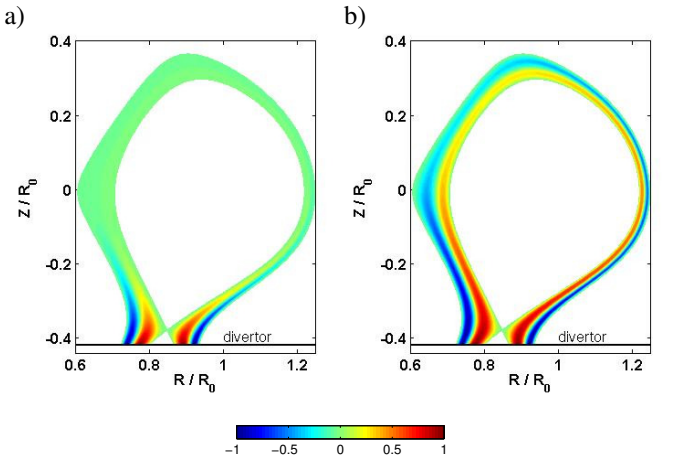

Figure 15: Snapshots of simulation with Dirichlet boundary condition $u|_b = \sin\left(2\pi\frac{\psi-\psi_{inner}}{\psi_{outer}-\psi_{inner}}\right)$ at divertor for time a) $t = 1$ and b) $t = 10$. 32 poloidal planes were employed with a perpendicular resolution of $h = 5 \cdot 10^{-4}$.

interior domain with the boundary condition:

$$u|_b = \sin\left(2\pi\frac{\psi - \psi_{inner}}{\psi_{outer} - \psi_{inner}}\right), \tag{24}$$

where ψ_{inner}, ψ_{outer} are the flux surface labels of the inner and outer limiting flux surfaces. From the snapshots, shown in fig. 15 it is obvious that the simulation approaches the final steady state $u = \sin\left(2\pi\frac{\psi-\psi_{inner}}{\psi_{outer}-\psi_{inner}}\right)$.

4.3. Further remarks

Finally, we want to note that among several different methods that we tried for the treatment of the boundaries, the one that we presented here turned out to be most robust and practical. We pass on a quantitative comparison but just list other approaches that we tried with its deficiencies.

- In an approach without ghost points a special treatment is applied to grid points which are connected to the boundary. On the corresponding side no interpolation is carried out but the desired boundary condition is set directly. The major drawback of the method is that if one wants to keep the interpolation stencil centered around map points, information from outside the domain is still required for those grid points whose map points are still in the interior domain but close to the boundary. So one either has to fall back to ghost points anyway in order to obtain the missing information, or one has to adapt the interpolation which is cumbersome and introduced other spurious numerical artefacts. Moreover, we found that the 'special' treatment of some points was causing corrugations within the poloidal plane.

- In analogy to Neumann boundary conditions we tried a treatment of Dirichlet boundary conditions according to fig. 11a, where the discrete parallel operator close to the boundary is not adapted, but the values on ghost points are also obtained via extrapolation according to (compare eq. (21)):

$$u_g = \frac{s_1\,(s_1+s_3)}{s_2\,(s_2-s_3)}u_g^+ - \frac{s_1\,(s_1+s_2)}{s_3\,(s_2-s_3)}u_g^{2+} + \left(1 + \frac{s_1^2 + s_1 s_2 + s_1 s_3}{s_2 s_3}\right)u_b, \tag{25}$$

where u_b is the prescribed value at the intersection of the magnetic field line with the boundary. However, we observed numerical instabilities in certain cases with this approach.

- On the other hand we tried to treat Neumann boundary conditions in analogy to Dirichlet boundary conditions according to fig. 11b, where ghost points are considered to be located on the boundary with the Taylor expansion adapted accordingly, such that

$$u_g = -\frac{s_3^2}{\left(s_2^2 - s_3^2\right)}u_g^+ + \frac{s_2^2}{\left(s_2^2 - s_3^2\right)}u_g^{2+} - \frac{s_2 s_3}{(s_2 + s_3)}u_b'. \tag{26}$$

However, also in this approach we observed numerical instabilities in certain cases.

- A setting of ghost points according to a first order Taylor expansion might not account for a variation of the distance to the boundary and corrugations within the poloidal plane were observed.

5. Conclusions

The flux-coordinate independent approach offers a viable solution to deal with complex geometries of magnetic fusion devices, especially a separatrix and X-point(s). The main challenge thereby is the discretisation of parallel operators as the numerical grid is not aligned with magnetic field lines.

We presented a new scheme for the parallel gradient which is based on a combination of interpolation and integration, where the degree of integration is controlled by a single parameter X. With respect to the pure interpolation scheme, which is also contained in the new scheme with $X = 0$, the additional effort required for implementation is very little and the increase in computational costs is practically negligible in the electrostatic case where the field line map does not evolve in time. In analogy to [1] the discrete parallel diffusion operator follows from the method of support operators. Whereas the pure interpolation scheme **S-3X0** exhibits erroneous corrugations which lead to a degradation of convergence, the new schemes approach a second order converge with toroidal resolution as the parameter X is gradually increased. Moreover, it was shown that the new scheme can even cope with strongly distorted maps. In contrast to non-aligned schemes, the presented aligned schemes allow an accurate treatment of flute modes at already very low toroidal resolutions. Thereby, the parallel diffusion operator discretised according to the support operator method **S-3X***X* exhibits a numerical perpendicular diffusion which is orders of magnitudes

lower than the naive discretisation method **D-3**. In conclusion the new **S-3X***X* schemes are the methods of choice as they were shown to be consistent, self-adjoint on the discrete level and therefore conserve energy, exhibit only very low numerical perpendicular diffusion, are computationally efficient and easy to implement. The scheme is implemented in the code GRILLIX, with which the benchmarks and examples for this paper have been produced, and has recently also been succesfully adopted in the code FELTOR, which is based on discontinuous Galerkin methods [2].

The accuracy of the interpolation is determined by perpendicular resolution. Structures that try to align along magnetic field lines might get a very small extent in the perpendicular direction due to magnetic shear. At some point they cannot be resolved by the perpendicular resolution any more, and the interpolation becomes inaccurate. However, at such small scales some perpendicular dynamics, i.e. perpendicular dissipation has to take over.

We also addressed the subtle issue of boundaries within the FCI approach, and presented a solution based on ghost points. The intersections of field lines with boundaries are identified during the field line tracing procedure. For Neumann boundary conditions values on ghost points are assigned according to a second order Taylor expansion along magnetic field lines around the intersection points, whereas in the case of Dirichlet boundary conditions the prescribed values are assigned directly. The extension of operators to ghost points is straight forward and fits very well into the established framework as the interpolation near the boundary has not to be adapted. We showed that with this solution the requested boundary conditions could be fulfilled provided that the perpendicular resolution is sufficient to resolve the structures, which might become strongly distorted due to the strong magnetic shear caused be the X-point.

All developed methods were implemented in the code GRILLIX and the application to a drift reduced Braginskii model [14] is aimed for the future in order to study edge/SOL turbulence around the separatrix.

6. Acknowledgements

The authors would like to thank L. Krönert for contributing to this work with useful discussions and fruitful comments. A part of this work was carried out using the HELIOS supercomputer system at Computational Simulation Centre of International Fusion Energy Research Centre (IFERC-CSC), Aomori, Japan, under the Broader Approach collaboration between Euratom and Japan, implemented by Fusion for Energy and JAEA. This work has been carried out within the framework of the EUROfusion Consortium and has received funding from the Euratom research and training programme 2014-2018 under grant agreement No 633053. The views and opinions expressed herein do not necessarily reflect those of the European Commission. The support from the EUROfusion Researcher Fellowship programme under grant number AWP16-ERG-MPG/Stegmeir is gratefully acknowledged.

[1] A. Stegmeir, D. Coster, O. Maj, K. Hallatschek, K. Lackner, Comput. Phys. Commun 198 (2016) 139.
[2] M. Held, M. Wiesenberger, A. Stegmeir, Comput. Phys. Commun 199 (2016) 29.
[3] W. D. D'haeseleer, W. N. G. Hitchon, J. D. Callen, J. L. Sohet, Flux Coordinates and Magnetic Field Structure, Springer Series in Computational Physics, Springer, 1990.
[4] M. Ottaviani, Phys. Lett. A 375 (2011) 1677.
[5] F. Hariri, M. Ottaviani, Comput. Phys. Commun. 184 (2013) 2419.
[6] F. Hariri, P. Hill, M. Ottaviani, Y. Sarazin, Phys. Plasmas 21 (2014) 082509.
[7] B. D. Dudson, J. Madsen, J. Omotani, P. Hill, L. Easy, M. Løiten, arxiv [physics.plasm-ph] 1602.06747v1.
[8] M. Shashkov, S. Steinberg, J. Comput. Phys. 118 (1995) 131.
[9] M. Shashkov, Conservative Finite-Difference Methods on General Grids, CRC Press, 1996.
[10] A. Stegmeir, D. Coster, O. Maj, K. Lackner, Contrib. Plasm. Phys. 54 (2014) 549.
[11] P. J. M. Carthy, Phys. Plasmas 6 (1999) 3554.
[12] P. C. Stangeby, The Plasma Boundary of Magnetic Fusion Devices, Institute of Physics Publishing, 2000.
[13] D. Farina, R. Pozzoli, D. D. Ryutov, Nucl. Fusion 33 (1993) 1315.
[14] A. Zeiler, J. F. Drake, B. Rogers, Phys. Plasmas 4 (1997) 2134.